Int. J. Rock Mech. Min. Sci. & Geomech. Abstr. Vol. 22, No. 1, pp. 31–38, 1985
Printed in Great Britain.

0148-9062/85 $3.00 + 0.00

Limit Analysis of Quasi-static Pyramidal Indentation of Rock

R. L. MICHALOWSKI*†

An approximate analysis of pyramidal indentation into a rock is presented in which the upper bound approach of limit analysis is utilized. The rock is assumed to obey the Mohr–Coulomb yield condition with a small tension cut-off. Two kinematically admissible mechanisms of possible deformation processes, based upon the non-associated flow rule, are adopted for predictions of gemoetrical variations. The phenomena experimentally observed in rocks, such as dilatancy and deterioration of strength while undergoing deformation, are accounted for approximately in the analysis. The kinematical approach of limit analysis to the problem of block-splitting under pyramidal indentation is also presented in the paper. A number of possible failure modes are examined and those which give the least upper splitting force are shown in detail.

Although the particular soluions presented have limited engineering capacity, the method proposed in the paper may find application in solving many rock engineering problems related to drilling, tunnelling, excavating, etc.

INTRODUCTION

A large number of theoretical studies have been devoted to the problem of quasi-static indentation of perfectly plastic materials. The solution to the plane problem of wedge indentation into an incompressible frictionless and weightless material was first given by Hill *et al.* [1], and into a dilational weightless material by Shield [2]. Similar formulation of the wedge indentation problem in relation to rock drillings was then presented by Cheatham [3], Pariseau and Fairhurst [4], and Paslay *et al.* [5]. Axi-symmetrical (conical) indentation into a frictional material has also been studied, usually in relation to the fall-cone test of soils, and pyramidal (and conical or spherical) indentation into a frictionless material in connection with hardness tests of metals.

The experimental research of stress–strain behaviour of rocks leads to the conclusion that rocks can be modelled as plastic bodies only to some extent. The plastic flow of rocks is observed under high hydrostatic pressures, while for low pressures very little plastic flow occurs prior to yielding by fracture. Thus, the formulations of a rock indentation problem based upon plastic behaviour seem to be appropriate for applications such as deep drilling below the earth's surface. Although the brittleness of rocks enables them to be modelled as perfectly plastic bodies only to some extent, the theorems of limit analysis were utilized by Chen and Drucker [6] and others [7, 8] in problems involving the analysis of rocks. Theoretical justification can be found in [6].

In the present paper, the upper bound theorem of limit analysis is used in order to estimate the force on a penetrating tetrahedral indenter. As the boundary of the raised material is part of the solution, the theorems of limit analysis (based on the principal of virtual work) are not directly applicable. In order to obtain the solution, the kinematics of the finite *process* of pentetration (including the shape of the moving boundary) is assumed, and the estimation of the penetration force has a sense of the upper bound for this assumed finite kinematics.

The next Section contains the description of the yield criterion and the flow rule used in the analysis, and also some remarks on work dissipation and density variation occurring on the velocity discontinuity surfaces. In the following Section, two kinematically admissible mechanisms of indentation are shown and some computational results are presented. The limit analysis (kinematical approach) of the bearing capacity of square blocks under pyramidal indentation is presented in the penultimate Section.

YIELD CRITERION, FLOW RULE AND WORK DISSIPATION

The Mohr–Coulomb failure criterion with a small tension cut-off, as shown in Fig. 1, is adopted in this paper. Parameters f_c' and f_t' denote the unconfined compressive and tensile strength, respectively. Compressive strength f_c' can be expressed in terms of co-

* Department of Civil and Mineral Engineering, University of Minnesota, 500 Pillsbury Drive, S.E., Minneapolis, MN 55455, U.S.A.
† Present address: Technical University of Poznan, Institute of Civil Engineering, Pl. M. Sklodowskiej-Curie 5, 60-965 Poznan, Poland.

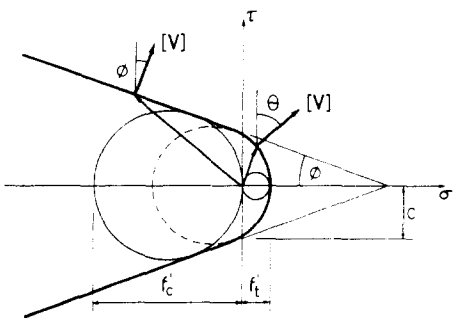

Fig. 1. The modified Mohr–Coulomb yield condition with a small tension cut-off.

hesion (c) and the internal friction angle (ϕ), namely

$$f_c' = \frac{2c\cos\phi}{1-\sin\phi}. \tag{1}$$

It is further assumed that the material is isotropic and initially homogeneous. The limit analysis method is based upon the idea of the perfectly plastic behaviour of solids in which the strain rate tensor $\dot{\varepsilon}_{ij}$ is related to the stress tensor σ_{ij} by the potential flow rule associated with the yield condition $F(\sigma_{ij})$

$$\dot{\varepsilon}_{ij} = \dot{\lambda}\frac{\partial F(\sigma_{ij})}{\partial\sigma_{ij}}, \quad \dot{\lambda} > 0, \tag{2}$$

where $\dot{\lambda}$ is a non-negative scalar function. For a material obeying a convex yield criterion $F(\sigma_{ij})$ and the flow rule in equation (2), the lower and upper bounds to the true value of the limit load can be rigorously proven [9]. When used in equation (2), the Mohr–Coulomb yield function provides much larger dilatancy than that observed experimentally in rocks. For that reason, it is postulated here that the material obeys the *non-associated* flow rule, and the location of the boundaries of the "piled-up" material are predicted from the kinematically admissible mechanism obeying such a rule. The plastic potential is assumed to have a form similar to the standard Mohr–Coulomb yield function, but with ϕ replaced by the dilation angle ϕ^* ($0 \leqslant \phi^* < \phi$). Although the limit analysis method is based on the idea of perfectly plastic behaviour of the material, the changes in strength are approximately incorporated into the analysis. The effect of hardening in the first stage of deformation of the material is neglected, and the parameters describing the strength of the virgin material correspond to the ultimate loading surface (failure criterion). The strength of the material is expected to deteriorate due to large strains and the creation and propagation of internal cracks. The material is treated as a continuum and, therefore, this deterioration of strength will be interpreted as strain-softening. In order to make the upper bound theorem applicable, the material is treated as perfectly plastic, with non-homogeneous local strength (caused, in fact, by the softening), and the *associated* flow rule in equation (2) is used for evaluation of the rate of work dissipation. The rate of energy dissipation, D_a per unit area of discontinuity surface for the modified Mohr–Coulomb failure function, as shown in Fig. 1, is from [6]

$$D_a = [\mathbf{V}]\left(f_c'\frac{1-\sin\theta}{2} + f_t'\frac{\sin\theta-\sin\phi}{1-\sin\phi}\right) = k[\mathbf{V}], \tag{3}$$

where $[\mathbf{V}]$ is the length of the velocity jump vector across the discontinuity surface and θ is shown in Fig. 1. The surface of the velocity discontinuity is usually interpreted in plasticity of dilational media as a mathematical approximation of a thin (but finite) material layer. Assigning a finite thickness to such a layer in incipient flow problems is necessary to preserve the finite dilation of the material. It was shown, however, by Drescher and Michalowski [10] that in problems treated as non-steady (pseudo-steady) flow processes rather than incipient mechanisms, the velocity discontinuity can be regarded as "shock" in dilating material, and the continuity condition and principle of mass conservation can be satisfied without assigning any thickness to the discontinuity. The flux of matter across the discontinuity surface has to satisfy the equation

$$[\rho \mathbf{V}^n] = 0, \tag{4}$$

where ρ is the density of the material and $\mathbf{V}^n$ is the normal component of the material speed of discontinuity propagation, and the brackets denote the jump. Equation (4) will be utilized in computations of density variations, although the influence of these variations on the distribution of gravitational forces will be neglected as the material is treated as weightless.

PYRAMIDAL INDENTATION INTO A ROCK

Two mechanisms of the process of tetrahedral indentation will be described in this Section. The first one, shown schematically in Fig. 2, consists of four identical flow areas, each adhering to one side of the tetrahedral pyramid (driving tool). An overall view of the material raised above the original plane surface xOy is shown in Fig. 2a, while half of the selected area of deformation (BOF in Fig. 2a) is shown in Fig. 2b. The mechanism is pseudo-steady; thus, any stage of deformation can be selected for the analysis of the kinematic field. Each of the four deformation areas consists of two rigid-motion regions. For the sake of clarity, the velocities (in cross-section ABCD) are shown separately in Fig. 3. While the pyramid KLMND is driven in the direction of the z-axis with the velocity $\mathbf{V}_0$, the region ACDF is moving with the velocity $\mathbf{V}_1$, causing relative sliding on the wall KLD of the pyramid. The region ACDF is separated from the virgin material by the triangle velocity discontinuity surface CDF. The second region, ABCF, moves with the velocity $\mathbf{V}_2$ and is separated from the first region by the surface of velocity discontinuity ACF, and from the virgin material by the surface BCF. The vectors $\mathbf{V}_1$, $\mathbf{V}_2$ and that of the velocity jump $[\mathbf{V}]$ along the surface ACF are parallel to the plane xOz. For the mechanism of the *process* to be kinematically admissible, it is necessary that $\mathbf{V}_1$, $\mathbf{V}_2$ and $[\mathbf{V}]$ satisfy the conditions: (i) $\mathbf{V}_1$ be compatible with $\mathbf{V}_0$, i.e. no overlap or gap along AFD will occur, and be inclined at the angle ϕ^* to the plane

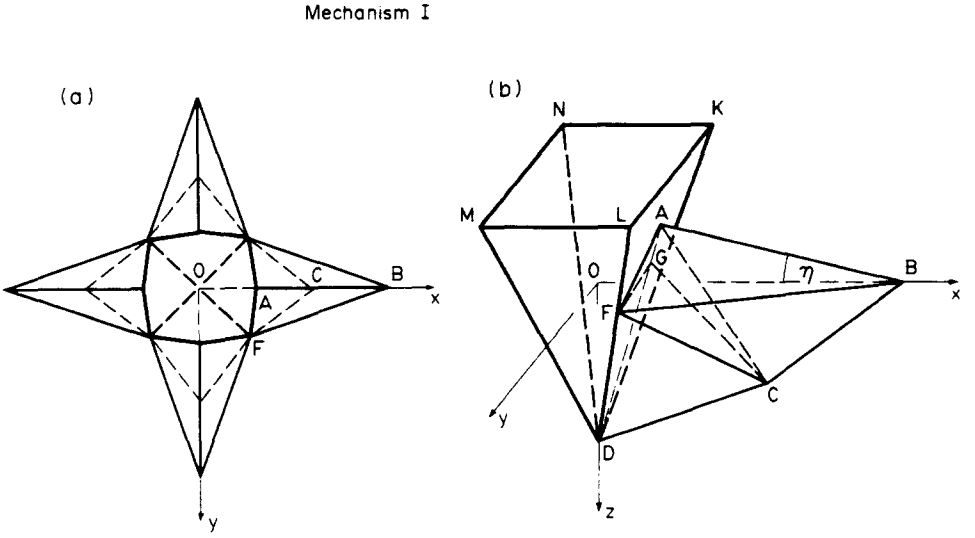

Fig. 2. Kinematically admissible mechanism (I) of pyramidal indentation, (a) overall view, (b) half of deformed area adhering to one side of the pyramid.

CDF; (ii) [V] be inclined at ϕ^* to the plane ACF; (iii) $\mathbf{V}_2$ be the sum of $\mathbf{V}_1$ and [V] and inclined at ϕ^* to BCF. These conditions allow for computing the angles λ_1, λ_2 and λ_3 (Fig. 3). The algorithm for obtaining the unknown angle η (Fig. 3) is similar to that shown by Hill *et al.* [1] for the pseudo-steady plane-strain process of wedge indentation, and the derived equation is given in Appendix I along with the expressions for velocities and angles λ_i ($i = 1, 2, 3$). After the angle η is obtained, the geometry of the deformed regions can be determined (for any stage of indentation) and the upper bound to the penetration force can be computed from the *incipient* kinematical mechanism associated with the yield function. The angles λ_i ($i = 1, 2, 3$) and the velocities for the incipient mechanism can be obtained from the same expressions as previously (Appendix I), but with the angle ϕ^* replaced by θ ($\phi \leqslant \theta \leqslant \pi/2$). Finally, the upper bound to the driving force for a pyramid with frictionless flanks can be written as

$$P^0 = \frac{8}{\mathbf{V}_0}[\mathbf{V}_1 k S^{\mathrm{CDF}} + \mathbf{V}_2 k S^{\mathrm{BCF}} + [\mathbf{V}] k S^{\mathrm{ACF}}], \qquad (5)$$

where k is given by equation (3) and S denotes the areas of discontinuity surfaces, respectively. When friction (ϕ_w) between the flanks of the pyramid and the rock is taken into consideration, the penetration force is

$$P = \frac{P^0}{1 - \dfrac{[\mathbf{V}]'}{\mathbf{V}_0}\dfrac{\sin\phi_w}{\sin(\beta + \phi_w)}}. \qquad (6)$$

The second mechanism of indentation, shown in Fig. 4, consists of four symmetrical areas separated by four cracks. The mechanism is again assumed to be pseudo-steady; thus, the cracks are expected to propagate according to the increasing depth of indentation. The deformed area shown in Fig. 4b (corresponding to the part BOB′ in Fig. 4a) consists of two rigid-motion regions: ACDC′, separated from the virgin material by the surface CDC′, with ADC′ being the crack surface; and ABCC′B′, separated from the virgin material by the surface BCC′B′ and with AB′C′ being the crack surface. Note that the region ACDC′ adheres to wall KLD of the pyramid only along the edge AD. Figure 3 can be adapted to analyse velocities, with angles λ_i ($i = 1, 2, 3$) replaced by ϕ^*, and the expressions in Appendix I can be adapted directly after substituting ϕ^* for λ_i. Further procedure in order to obtain the upper limit load is the same as in the case of the first mechanism considered, and for frictionless sides of the pyramid yields

$$P^0 = \frac{8}{\mathbf{V}_0}[\mathbf{V}_1 k S^{\mathrm{CDC'}} + \mathbf{V}_2 k S^{\mathrm{BCC'B'}} + [\mathbf{V}] k S^{\mathrm{ACC'}}], \qquad (7)$$

[for a frictional pyramid see equation (6)]. Propagation of the macro-cracks was assumed here as part of the kinematically admissible mechanism of deformation; the work dissipated on the crack's front was, however, neglected in the analysis. In mechanisms with rigid-motion regions such as considered here, a velocity discontinuity adjacent to the crack tip must exist in order for the velocity field with the crack propagation to be admissable (Fig. 5). Assigning the critical stress following from the yield criterion (Fig. 1) to the tensile zone

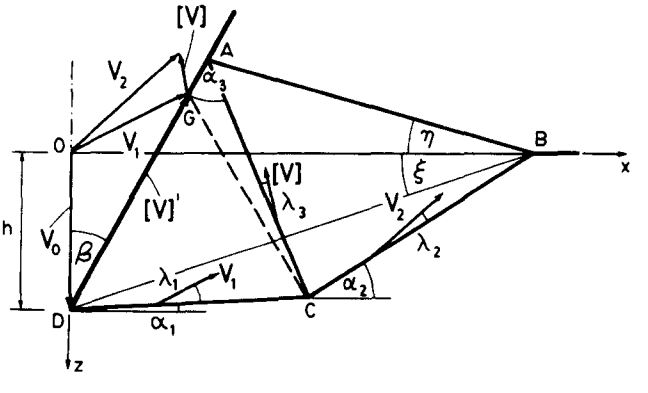

Fig. 3. Hodograph (velocity vector diagram) for the mechanism of indentation.

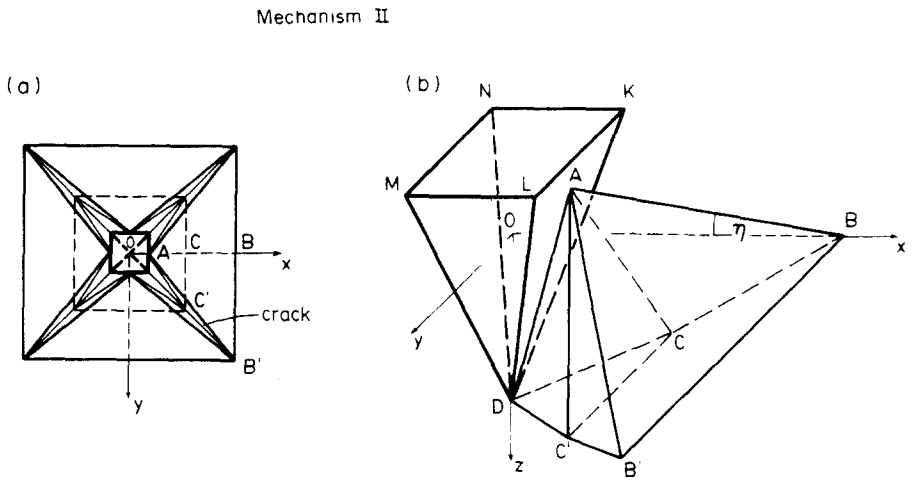

Fig. 4. Mechanism of indentation (II) with four macro-cracks, (a) overall view, (b) part of the deformed regions.

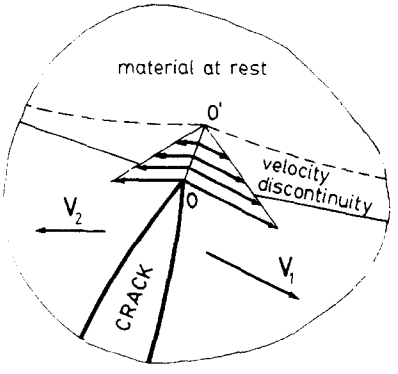

Fig. 5. Crack in a plane kinematically admissible velocity field.

OO′ (with a length dependent on the plastic deformability of the material in tension) preceding the crack opening, the rate of work dissipation due to the crack growth can be approximately determined and added to the total rate of work dissipation in the analysis.

In the examples computed, angles α_i (Fig. 3) in both mechanisms were optimized in order to obtain the least upper penetration force ($P^{\min}$); the material was treated as weightless and, therefore, angles α_i corresponding to $P^{\min}$ were independent of the depth of indentation. The material parameters of the rock were the internal friction angle ϕ, cohesion c and the ratio of unconfined compressive strength to unconfined tensile strength f_c'/f_t'. Such a set of parameters is equivalent to ϕ, f_c' and f_t' [see equation (1)]. Both mechanisms of indentation were assumed to be pseudo-steady and, consequently, the penetration force can be expressed in a dimensionless form (for given β, ϕ, ϕ^* and ϕ_w)

$$F = \frac{P}{ch^2}, \tag{8}$$

where P is the penetration force and h is the depth of indentation. Some computational results are shown in Fig. 6a and b. The results were not obtained for any particular kind of material for which the physical strain–strength relation is given. Therefore, the deterioration of strength was taken into account approximately, by assuming that the cohesion c' of the material within the deformed regions is

$$c' = \omega c \quad (0 \leqslant \omega < 1), \tag{9}$$

where c is the cohesion of the virgin material. This results in a smaller contribution of work dissipation along the velocity discontinuities within the deformed material. In the calculations of the work-dissipation along the surfaces separating the virgin material from the deformed regions, the strength of the virgin material was used. In the examples computed, the angle of dilation was assumed to be $\phi^* = 5°$ along the discontinuity surfaces separating the deformed regions from undisturbed material, and $\phi^* = 0$ (incompressibility) within the deformed regions. Numerical procedure showed that the least upper limit to the penetration force for both mechanisms corresponds to the angle $\theta = \phi$. It is seen from Fig. 6 that, depending on the included half-angle β of the pyramid, for given material parameters, either mechanism I or mechanism II may yield the lower value of the penetration force. Further computations showed that the range of β for which mechanism II yields a lower estimation of the penetration force increases with the increase of ϕ and/or ϕ_w.

Although the density of the material prior to deformation was assumed homogeneous, three regions of

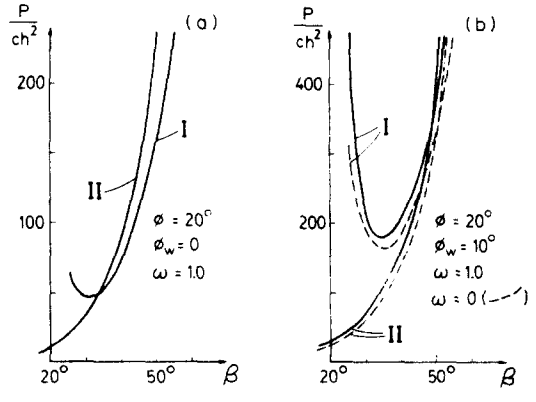

Fig. 6. Force of penetration (dimensionless) vs the included half-angle of the pyramidal indenter.

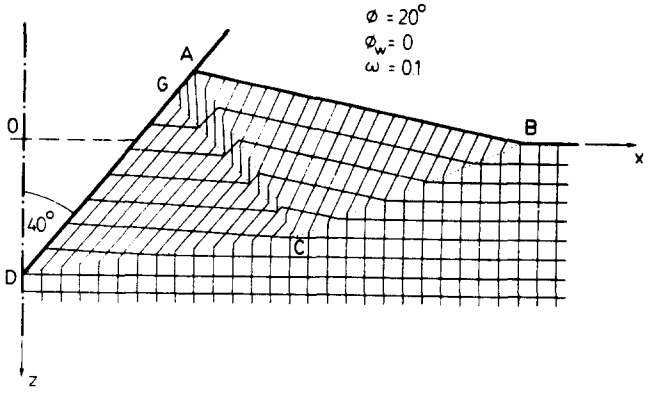

Fig. 7. Deformation of the originally square material grid in the plane of symmetry xOz, corresponding to the mechanism of deformation shown in Fig. 2.

different denstiy can be distinguished within the deformed area for both mechanisms. Creation of the regions with different density will be explained here only for mechanism I; however, the same reasoning can be extended for the second mechanism. The three regions of different density, shown in Fig. 2b, are: GCDF with the density ρ_1, ABCF with the density ρ_2, and ACGF with ρ_3. The dilation of the material within the region GCDF occurred exclusively across the propagating discontinuity surface CDF. Similarly, dilation of the material within the region ABCF occurred across discontinuity surface BCF. The material in the third region, ACGF, first dilated along the surface BCF and then was subjected to additional dilation while passing the surface ACF. Deformation of the originally square material grid in the plane of symmetry xOz is shown in Fig. 7. The speeds of propagation of the discontinuity surfaces were computed from the geometrical relations in Fig. 2b and Fig. 3 (as functions of $\mathbf{V}_0$) and equation (4) was used in order to compute ρ_1, ρ_2 and ρ_3. In the examples, the angle ϕ^* within the deformed region was taken as 0; hence it is obvious that in such a case $\rho_2 = \rho_3$. In the examples where $\beta = 30°$, $\phi = 20°$, $\phi_w = 10°$, $\omega = 0$ and the density of the virgin material $\rho_0 = 2.00$ (Mg/m^3), the densities ρ_1 and $\rho_2 = \rho_3$ were: 1.80 and 1.83 for mechanism I and 1.89 and 1.94 (Mg/m^3) for mechanism II, respectively.

FRAGMENTATION OF A BLOCK SUBJECTED TO PYRAMIDAL INDENTATION

If indentation into a finite block of rock takes place, the mechanisms of penetration discussed in the previous Section can be considered only to a certain extent. At some stage of indentation, the block is likely to fail by splitting into smaller blocks. It is assumed that sufficient plastic deformability (both compressive and tensile) exists to permit the application of the limit theorems to the rocks under consideration. In this Section, some of the kinematically admissible mechanisms for block-splitting are examined and the kinematical approach of limit analysis is applied in order to estimate the load necessary to produce fragmentation of the block. The same approach was applied earlier by Chen and Drucker [6] in order to evaluate the bearing capacity of blocks under strip or square loads.

Fifteen mechanisms of possible fragmentation of blocks with square bases were considered. Six of them are shown schematically in Fig. 8. The velocities and the contours of the material raised above the original top plane of the blocks during indentation, and the regions of the deformed material within the blocks are not shown in the figures deliberately, in order to preserve the clarity of the failure modes. The penetrating tetrahedral pyramid is treated as a tool driven with only the vertical velocity component being controlled. Thus, the failure mode of the block can be either symmetrical (with respect to two planes), such as shown in Fig. 8b, c and e, or like the ones in Fig. 8a, d and f in which the limit load is still vertical but the tool "chooses" a non-vertical velocity when failure occurs. In the examples computed the best upper estimations of the splitting force for high blocks were obtained from mechanism (a), and for short blocks from mechanism (e).

Fragmentation of blocks is treated here as an incipient flow problem and therefore only the velocity field associated with the yield function is now of our interest. Figure 9a shows the cross-section of the failure mechanism shown in Fig. 8a, corresponding to the plane ABCD. Part of the block, AGBG'E'CED, is assumed to

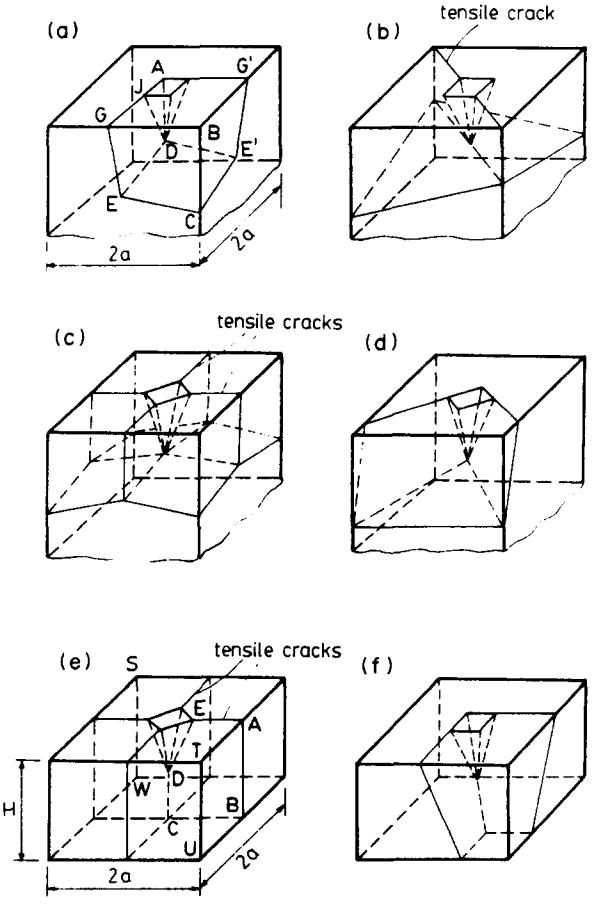

Fig. 8. Kinematically admissible failure modes for blocks under pyramidal indentation. The contours of the material raised above the original top surface of the blocks and the regions of material deformed during indentation are not shown in order to preserve the clarity of the failure modes.

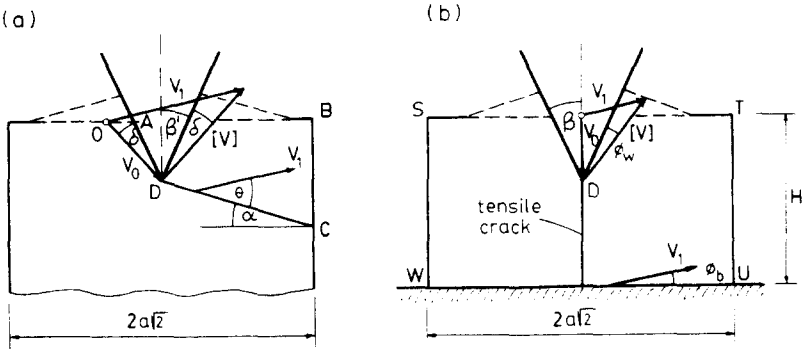

Fig. 9. Hodographs (velocity vector diagrams) for the failure modes (a) and (e) from Fig. 8.

move as a rigid block with the velocity $\mathbf{V}_1$ parallel to the plane ABCD. The Coulomb friction on the sides of the pyramid is incorporated into the analysis using the method suggested by Collins [11]. A "fictitious" incipient velocity field is assumed, such that the velocity vector $\mathbf{V}_0$ of the moving pyramid is inclined to the planes ADEG and ADE'G' at the angle of Coulomb friction ϕ_w, and vector [V] of relative sliding on the two flanks adhering to the rigid-motion region is inclined to these flanks also at the angle ϕ_w (for angle δ in Fig. 9a see Appendix II). Such a velocity field provides that the rate of work dissipation due to the Coulomb friction on the flanks is equal to zero. For known α and θ, an angle θ' of inclination of vector $\mathbf{V}_1$ to the planes ADEG and ADE'G' can be found and, finally, the upper bound to the true limit load can be expressed as

$$P = \frac{V_1}{V_0}[k(\theta)S^{CEDE} + 2k(\theta')S^{DEGJ}], \qquad (10)$$

where k is given by equation (3), and V_1 and θ' are given in Appendix II. Geometrical changes and deterioration of the strength of the material due to the process of indentation prior to the fragmentation of the block should be incorporated into the analysis. It is obvious that if the second mechanism of indentation (Fig. 4) occurs prior to the failure mechanism shown in Fig. 8a, the plane DEGJ intersects the virgin material as well as the deformed material raised above the original top plane surface of the block (not shown in Fig. 8a), the deformed regions within the block and the crack. The part of the cross-section due to the crack should be excluded from the area S^{DEGJ} in equation (10), and part of the cross-section due to the material raised above the original top surface should be included. Further, if the cohesion of the material is assumed to drop due to the deformation during the process of indentation, only the fraction ω [see equation (9)] of the cross-section through the deformed material should be included in S^{DEGJ}. If the first mode of indentation (Fig. 2) takes place before the failure mechanism shown in Fig. 8a, the plane DEGJ intersects only the virgin material of the block and S^{DEGJ} in equation (10) is exactly the area shown in Fig. 8a. In the examples computed, angles α and θ ($\phi \leqslant \theta \leqslant \pi/2$) were optimized in order to obtain the least upper limit force (P^{min}). It was found that for all examples P^{min} corresponds to $\theta = \phi$.

For relatively short blocks, mechanism (e) gives lower estimations of the upper bound to the true limit load than mechanism (a). The hodograph for that mechanism is relatively simpler (Fig. 9b). In order to include the base friction, vector $\mathbf{V}_1$ is assumed to be inclined to the base at the angle of friction ϕ_b (the contribution to the work dissipation due to the base friction could be, in this case, expressed explicitly). The upper bound to the true limit load for the mechanism shown in Fig. 8e can be expressed as

$$P = \frac{4\sqrt{2}\tan(\beta + \phi_w)}{1 - \tan(\beta + \phi_w)\tan\phi_b} f_t' S^{ABCDE}, \qquad (11)$$

where f_t' is the unconfined tensile strength. It should be noted that, if the second mode of indentation (Fig. 4) occurs prior to the failure mechanism shown in Fig. 8e, then the area S^{ABCDE} in equation (11) should be reduced by the area of the crack being intersected by the plane ABCDE.

Some computational results for selected data are shown in Fig. 10. The thick parabolic curves describe the increase of the penetration force due to the increasing depth of indentation h. Simultaneously solving the least upper bound to the force of penetration and expressions (10) or (11) (broken lines) yields the approximate load and depth of indentation corresponding to the failure of the block (small circles in Fig. 10). Figure 10 indicates that (for given data) mechanism (a) yields a better

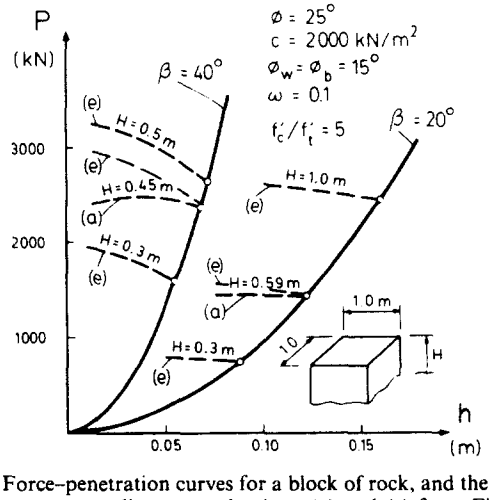

Fig. 10. Force–penetration curves for a block of rock, and the splitting forces corresponding to mechanisms (a) and (e) from Fig. 8.

(lower) estimation of the splitting force than mechanism (e) for $\beta = 40^\circ$ and blocks higher than 0.45 m, and for $\beta = 20^\circ$ and blocks higher than 0.59 m.

CONCLUSIONS

The problem of pyramidal indentation into a rock was solved approximately using the upper bound approach of limit analysis. The first mechanism considered was similar to one used in metal plasticity [12]. It is surprising to notice that for the material whose yield criterion is a function of hydrostatic prssure this mechanism yields increasing penetration force with decreasing half-angle of the pyramid β (for a certain range of β). A kinematically admissible velocity field of this shape cannot be constructed for small angles β and $\phi > 0$. Incorporating macro-cracks into the mechanism of deformation (Mechanism II) provides kinematical admissibility also for small β. The mechanism with propagating macro-cracks provides values of the penetration force lower than Mechanism I for a broad range of β (depending on material properties). The deterioration of strength, as approximately incorporated into the analysis, has no major effect on the penetrating force since in the mechanisms considered the majority of the work is dissipated along the discontinuity surfaces moving into the virgin material.

The solution to the problem of indentation presented in the paper may be useful in evaluating forces involved in hollowing and fragmentation of rocks, wherever the rock-crushing is done by pyramidal indentations. The diagrams, as shown in Fig. 6, can be used for predicting the force on a single bit necessary to proceed with the process of hollowing. An example where the prediction of block splitting by a pyramidal tool is carried out was also presented. The unconfined compressive strength of the block used in the example was 6279 kN ($f_c' \times$ area of the block). It is seen from Fig. 10 that the force necessary to split the block can be very effectively reduced when it is applied through the pyramidal indenter. Results of computations confirm the "common-sense" supposition that the block-splitting force decreases with the decrease of the angle of the pyramid. The extension of the analysis to other than square base pyramids and different shapes of blocks, including false-nose formations, and further refinement of the failure modes based on experiments may enable the analysis to be useful in size-reduction operations in which a required shape of rock fragments is desired.

The presented solutions to rock indentation and block splitting problems have limited engineering application. It is believed, however, that the method proposed in this paper, although approximate in its nature, may find application in solving many rock engineering problems related to drilling, tunnelling, excavating, etc. It should be noticed that the procedure used for tracing the kinematics of the deformation process by means of kinematically admissible (non-associated) velocity fields may become progressively less accurate as deformation proceeds. Therefore, for obtaining realistic results, experimental verification of the velocity fields is recommended. Incorporating the strength deterioration of rock into the analysis, as proposed, may impose some limitations as to the type of rock for which the analysis can be applied.

Acknowledgements—The author would like to thank the Council for International Exchange of Scholars and the University of Minnesota for making his research possible.

Received 20 *January* 1984; *revised* 7 *May* 1984.

REFERENCES

1. Hill R., Lee E. H. and Tupper S. J. The theory of wedge indentation of ductile materials. *Proc. R. Soc. A* **188**, 273–289 (1947).
2. Shield R. T. Mixed boundary value-problems in soil mechanics. *Q. appl. Math.* **11**, 61–75 (1953).
3. Cheatham J. B. Jr. An analytical study of rock penetration by a single bit tooth. *VIIIth Annual Drilling and Blasting Symp.*, Univ. of Minnesota (1958).
4. Pariseau W. G. and Fairhurst C. The force-penetration characteristic for wedge penetration into rock. *Int. J. Rock Mech. Min. Sci.* **4**, 165–180 (1967).
5. Paslay P. R., Cheatham J. B. Jr and Fulcher C. W. G. Plastic flow of rock under a pointed punch in plane strain. *J. appl. Mech.* **35**, 95–101 (1968).
6. Chen W. F. and Drucker D. C. Bearing capacity of concrete blocks or rock. *J. Engng Mech. Div. Am. Soc. civ. Engrs* **95**, 955–978 (1969).
7. Lippmann H. Plasticity in rock mechanics. *Int. J. mech. Sci.* **13**, 291–297 (1971).
8. Giger M. W. and Krizek R. J. Estimate for bearing capacity of a prismatic pillar. *Rock Mech.* **9**, 189–211 (1977).
9. Drucker D. C., Greenberg H. J. and Prager W. Extended limit design theorems for continuous media. *Q. appl. Math.* **9**, 381–389 (1952).
10. Drescher A. and Michalowski R. L. Density variation in pseudo-steady plastic flow of granular media. *Géotechnique* **34**, 1–10 (1984).
11. Collins I. F. The upper bound theorem for rigid/plastic solids generalized to include Coulomb friction. *J. Mech. Phys. Solids* **17**, 323–338 (1969).
12. Haddow J. B. and Johnson W. Indenting with pyramids—I. Theory. *Int. J. mech. Sci.* **3**, 229–238 (1961).

APPENDIX I

The angle η (Fig. 3) can be iteratively evaluated from the equation

$$\mathbf{V}_0 \frac{\sin \eta}{\tan \xi} - \mathbf{V}_2 \sin(\eta + \alpha_2 + \lambda_2) = 0.$$

The velocities $\mathbf{V}_1$, $\mathbf{V}_2$, [V] and [V]′, shown in Fig. 3, are

$$\mathbf{V}_1 = \mathbf{V}_0 \frac{\sin \beta}{\cos(\beta + \alpha_1 + \lambda_1)},$$

$$\mathbf{V}_2 = \mathbf{V}_1 \frac{\cos(\beta + \alpha_1 - \alpha_3 + \lambda_1 + \lambda_3)}{\cos(\beta + \alpha_2 - \alpha_3 + \lambda_2 + \lambda_3)},$$

$$[\mathbf{V}] = \mathbf{V}_1 \frac{\sin(\alpha_2 - \alpha_1 + \lambda_2 - \lambda_1)}{\cos(\beta + \alpha_2 - \alpha_3 + \lambda_2 + \lambda_3)},$$

$$[\mathbf{V}]' = \mathbf{V}_0 \frac{\cos(\alpha_1 + \lambda_1)}{\cos(\beta + \alpha_1 + \lambda_1)}.$$

The angle ξ (Fig. 3) is analytically described as a function of η

$$\tan \xi = (\cos \beta - B \sin \eta)/(B \cos \eta + \sin \beta),$$

$$B = [\cos(\beta + \alpha_1) \cos(\alpha_2 + \beta - \alpha_3)]/[\sin(\alpha_2 + \eta) \cos(\alpha_3 - \alpha_1 - \beta)].$$

Angles λ_i ($i = 1, 2, 3$) can be obtained from the relation

$$\sin \lambda_i = \sin \phi^*/\sin \mu_i, \quad i = 1, 2, 3,$$

where

$$\tan \mu_1 = \sin \beta / \cos (\beta + \alpha_1),$$
$$\tan \mu_2 = \tan \beta \tan \xi / [\sin \alpha_2 (1 - \tan \beta \tan \xi)],$$
$$\tan \mu_3 = \tan \mu_2 \sin \alpha_2 \cos (\beta - \eta) / (\sin \alpha_3 \sin \eta).$$

APPENDIX II

The velocity $\mathbf{V}_1$ in Fig. 9a is

$$\mathbf{V}_1 = \mathbf{V}_0 \frac{\sin 2(\beta' + \delta)}{\cos (\beta' + \delta + \theta - \alpha)},$$

where

$$\sin \delta = \sin \phi_w \sin 2\beta'' / \sin \beta'.$$

and

$$\tan \beta' = \sqrt{2} \tan \beta, \quad \tan \beta'' = \sin \beta.$$

The angle θ' of inclination of vector $\mathbf{V}_1$ to the planes ADEG and ADE'G' (Fig. 8a) can be computed from the relation

$$\sin \theta' = \sin \beta' \cos (\theta - \beta' - \alpha) / \sin 2\beta''.$$